ADVANCED FUNCTIONAL MATERIALS
www.afm-journal.de

Materials Views
www.MaterialsViews.com

Tunable Magnonic Spectra in Two-Dimensional Magnonic Crystals with Variable Lattice Symmetry

*Susmita Saha, Ruma Mandal, Saswati Barman, Dheeraj Kumar, Bivas Rana, Yasuhiro Fukuma, Satoshi Sugimoto, YoshiChika Otani, and Anjan Barman**

Tunable magnonic properties are demonstrated in two-dimensional magnonic crystals in the form of artificial ferromagnetic nanodot lattices with variable lattice symmetry. An all-optical time-domain excitation and detection of the collective precessional dynamics is performed in the strongly magnetostatically coupled $Ni_{80}Fe_{20}$ (Py) circular dot lattices arranged in different lattice symmetry such as square, rectangular, hexagonal, honeycomb, and octagonal symmetry. As the symmetry changes from square to octagonal through rectangular, hexagonal and honeycomb, a significant variation in the spin wave spectra is observed. The single uniform collective mode in the square lattice splits in two distinct modes in the rectangular lattice and in three distinct modes in the hexagonal and octagonal lattices. However, in the honeycomb lattice a broad band of modes are observed. Micromagnetic simulations qualitatively reproduce the experimentally observed modes, and the simulated mode profiles reveal collective modes with different spatial distributions with the variation in the lattice symmetry determined by the magnetostatic field profiles. For the hexagonal lattice, the most intense peak shows a six-fold anisotropy with the variation in the azimuthal angle of the external bias magnetic field. Analysis shows that this is due to the angular variation of the dynamical component of magnetization for this mode, which is directly influenced by the variation of the magnetostatic field on the elements in the hexagonal lattice. The observations are important for tunable and anisotropic propagation of spin waves in magnonic crystal based devices.

1. Introduction

Magnetic nanostructures form the basis of many present and future technologies including patterned magnetic media,[1] magnetic random access memory,[2] magnetic logic devices[3,4] and magnetic resonance imaging.[5] The patterned magnetic media uses two-dimensional arrays of lithographically patterned magnetic islands (bits) and the magnetic switching behaviors of such systems including switching field distribution have been thoroughly studied. An essential criterion has been to eliminate the magnetostatic interaction (cross-talks) between the individual bits for the application in patterned magnetic media. Similar arrays of nanomagnets may be used to propagate high frequency magnetic excitations in the form of collective long wavelength spin waves as information carries in magnonic crystals, when the magnetic elements are strongly magnetostatically coupled. Such coupled arrays of nanomagnets undergo a collective dynamics,[6–12] where the individual nanomagnets maintain constant amplitude and phase relationships, and show rich magnonic band structures with tunable bandgap properties. Thereby a new field of research known as magnonics[13–15] has been introduced, which has potential to use spin waves to carry and process information and also in building nanoscale microwave components such as filters, attenuators and phase shifters.[16] Emerging new field such as coherent oscillation of an array of spin torque nano-oscillators[17,18] also promises to act as on-chip microwave sources for electronic and magnetoelectronic applications.

Two-dimensional ferromagnonic dot lattices have been extensively fabricated and studied in recent years. Various physical parameters of the lattices such as lattice constants, and shape, size and material of the magnetic dots have been varied to tailor the magnonic properties in those lattices. The high frequency magnetization dynamics of such lattices have been studied experimentally by time domain,[6,7,19] frequency domain,[8] wave vector domain[9–12] techniques and by analytical methods[20,21] and micromagnetic simulations.[22] The frequency, damping and spatial profiles of collective modes and the dispersion of their frequency with wavevector have been studied with the variation

S. Saha, R. Mandal, Dr. S. Barman, D. Kumar, B. Rana, Prof. A. Barman
Department of Condensed Matter Physics and Material Sciences
S. N. Bose National Centre for Basic Sciences
Block JD, Sector III, Salt Lake, Kolkata 700098, India
E-mail: abarman@bose.res.in
Prof. Y. Fukuma, S. Sugimoto, Prof. Y. Otani
Advanced Science Institute
RIKEN, 2-1 Hirosawa,
Wako, Saitama 351-0198, Japan
S. Sugimoto, Prof. Y. Otani
Institute for Solid State Physics
University of Tokyo
5-1-5 Kashiwanoha, Kashiwa, Chiba 277-8581, Japan
Prof. Y. Fukuma
Frontier Research Academy for Young Researchers
Kyushu Institute of Technology
Iizuka, Fukuoka 820-8502, Japan

DOI: 10.1002/adfm.201202545

of above parameters. In addition to the periodicity of the lattice, the interdot magnetostatic interactions in the lattices play a very important role in determining the collective magnonic modes in these lattices and further tailoring of this interaction field offers exciting prospects in magnonics. The variation of lattice symmetry is an attractive option, by which the magnetostatic fields of highly complex nature can potentially be introduced but it has hitherto not been tried in the context of the spin wave dynamics of magnonic crystals. The quasistatic magnetization processes of nanomagnets arrays with different symmetry have been reported by static magneto optical Kerr effect measurements.[23–25] A configurational anisotropy has been observed from the dependence of the hysteresis loops with the angle of the in-plane magnetic field with respect to the symmetry of the array. On the other hand, magnetization dynamics of magnetic antidot lattices with varying lattice symmetry has been reported by a combination of Brillouin light scattering and ferromagnetic resonance measurements.[26] In all lattices the eigenfrequencies show angular dependence consistent with the symmetry of the lattice. However, no report on the dependence of the magnetization dynamics in ferromagnetic dot lattices on the lattice symmetry could be found in the literature. Here, we present an all-optical excitation and detection of magnetization dynamics in closely packed circular $Ni_{80}Fe_{20}$ (Py) dot lattices arranged in different lattice symmetry. The spin wave spectra show a significant variation as the symmetry is reduced from square lattice to octagonal lattice through the rectangular, hexagonal and honeycomb lattices. We also investigate the anisotropy of the collective modes in the hexagonal lattice as a function of the azimuthal angle (φ) of the in-plane bias magnetic field.

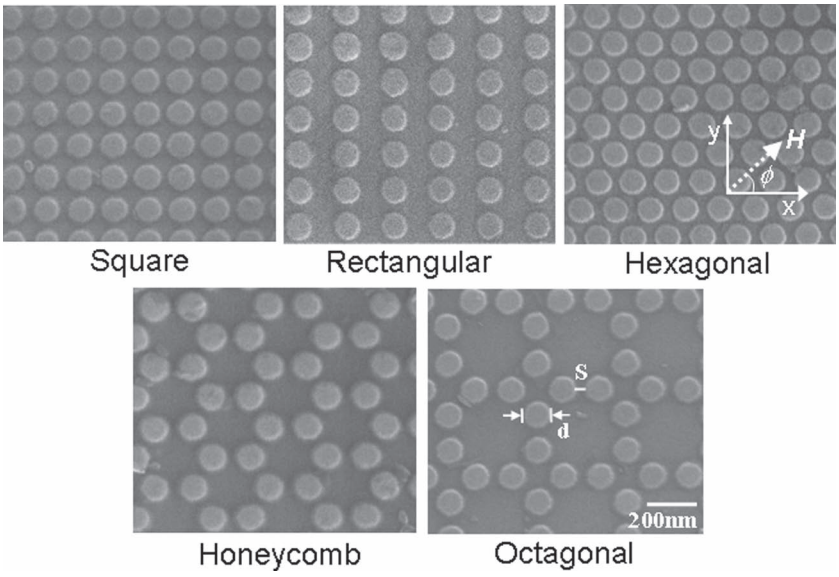

Figure 1. Scanning electron micrographs of the permalloy dot lattices with different lattice symmetry, namely square, rectangular, hexagonal, honeycomb, and octagonal symmetry. The dot diameter and separation are shown in the micrograph for the octagonal lattice along with the length scale bar. The geometry of the applied magnetic field for all lattices is shown in the micrograph of the hexagonal lattice.

2. Result and Discussion

10 μm × 10 μm lattices of 20-nm-thick Py dots with circular shapes arranged in different lattice symmetry were fabricated by a combination of electron-beam lithography and electron-beam evaporation. The diameter of the dots is about 100 nm with maximum ±10% deviation within different lattices. The edge to edge separation between the dots is about 30 nm with maximum ±10% deviation within different lattices. The sizes of the dots are chosen in such a way that the individual dots can support both the centre and edge modes of precession of magnetization. The edge to edge separation is chosen in such a way that the dots are strongly magnetostatically coupled and show collective modes of precession. The dots are chosen to be of circular shapes so that the individual dots do not posses any configurational anisotropy[27] due to their shapes.

Both two-dimensional Bravais (square, rectangular, hexagonal) and non-Bravais (honeycomb, octagonal) lattices are chosen here to investigate the effects of variation of translational symmetry of the lattice and finally symmetry breaking on the magnonic spectra. **Figure 1** shows the scanning electron micrographs of all types of lattices. The small deviation in size and separation from the nominal dimensions as obtained from the micrographs will eventually be included in the micromagnetic simulations. The chemical compositions of the dots measured by the energy dispersive X-ray spectroscopy agree well with the nominal composition of the target material. The height profiles of the dots were measured by atomic force microscope and the average height was found to be between 20 and 22 nm in different lattices, which agree well with the nominal thickness of the samples. The ultrafast magnetization dynamics of the samples are measured by using a custom built time-resolved magneto optical Kerr effect microscope based upon a two color collinear pump-probe setup.[28] The magneto-optical Kerr rotation of the probe beam (λ = 800 nm, pulsewidth ≈ 70 fs) is measured after excitation by the pump beam (λ = 400 nm, pulsewidth ≈ 100 fs) as a function of the time delay between the pump and probe beams. A bias field of variable amplitude is applied to the sample, the direction of which was tilted slightly out of the plane of the sample to have a finite demagnetizing field along the direction of the pump pulse. The component of the bias field in the sample plane is referred to as H as shown in Figure 1. The pump pulse rapidly modifies the out-of-plane demagnetizing field and thereby induces precessional magnetization dynamics within the dots.[29,30]

2.1. Variation of Precessional Dynamics with the Symmetry of the Nanodot Lattices

Figure 2 shows the typical time-resolved reflectivity and Kerr rotation data from a Py dot lattice arranged in a hexagonal lattice

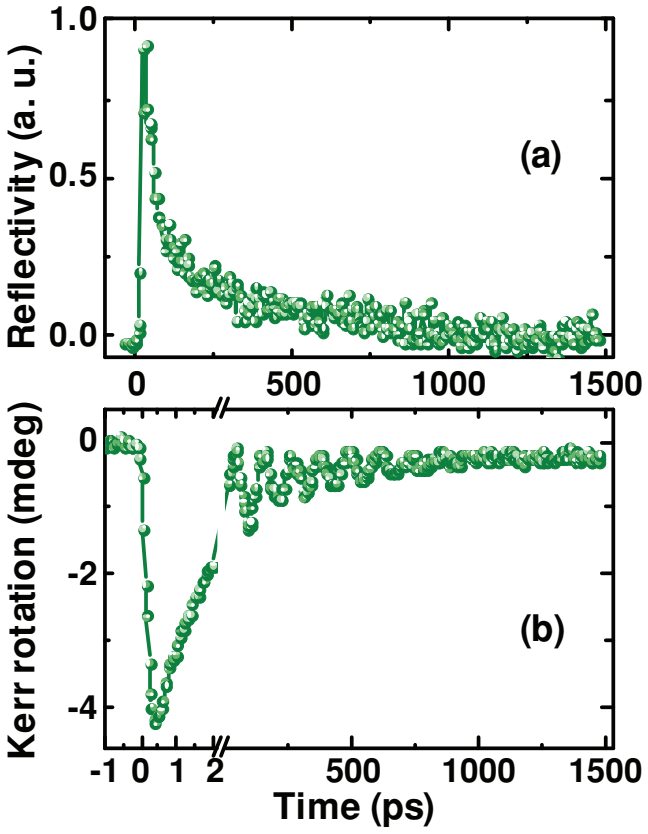

Figure 2. Typical time-resolved a) reflectivity and b) Kerr rotation data are shown for the Py dot lattice with hexagonal lattice symmetry at H = 1.3 kOe at $\varphi = 0°$.

symmetry at a bias field H = 1.3 kOe at φ = 0°. The reflectivity shows sharp rise followed by a bi-exponential decay, whereas the time-resolved Kerr rotation shows a fast demagnetization[31] within 500 fs with a bi-exponential decay with decay constants of about 2 ps and 500 ps. The precessional dynamics appears as an oscillatory signal on the slowly decaying part of the time-resolved Kerr rotation data. A fast Fourier transform (FFT) is performed after subtracting the bi-exponential background to find out the corresponding power spectra. The measurement time window of 1.5 ns used in this experiment is a compromise between the total measurement time, which is determined by the number of scan points and the integration time of the lock-in amplifier for each scan point, and the time taken to cause a slow drift of the piezoelectric sample scanning stage. Nevertheless, this 1.5 ns time window is found to be sufficient to resolve the spin wave spectra for different lattices.

Figure 3a,b show the background subtracted experimental time resolved Kerr rotations for lattices with different lattice symmetry and the corresponding power spectra. From the experimental data a clear variation in the spin wave dynamics is observed with the lattice symmetry. For the square lattice the time-domain data shows a damped single frequency oscillation, which transforms into a single sharp peak in the frequency domain. However, as the symmetry reduces in the rectangular lattice a mode splitting appears. The high intensity peak shifts slightly towards the lower frequency while a low intensity peak appears at a slightly higher frequency. In the case of hexagonal lattice a dramatic change occurs and three clear peaks are observed in the FFT spectrum as a consequence of the highly nonuniform oscillations in the time-resolved Kerr signal. The peak at the centre has the highest intensity, while the peak at the higher frequency is also significantly intense as compared to the main peak. The third peak is of very low intensity, which appears at a much lower frequency with about 3.5 GHz shift from the main peak. The time-resolved Kerr rotation and the corresponding FFT spectrum for the honeycomb lattice are even more complicated. The time-resolved data dephases rapidly after about 3 cycles of oscillation leaving a small amplitude nonuniform oscillation, while a broad band of modes are observed between 1 and 14 GHz in the FFT spectrum. Seven peaks are observed, where the central peak is very broad with a partial splitting. In the octagonal lattice three closely spaced peaks are observed between 7 and 11 GHz, while a low intensity band is observed below 5 GHz.

We have performed micromagnetic simulations using the OOMMF software[32] by considering finite lattices of about 1100 nm × 1100 nm × 20 nm volumes consisting of circular dots arranged in different lattice symmetry. We have done test simulations to see if the artificial boundaries of the simulated

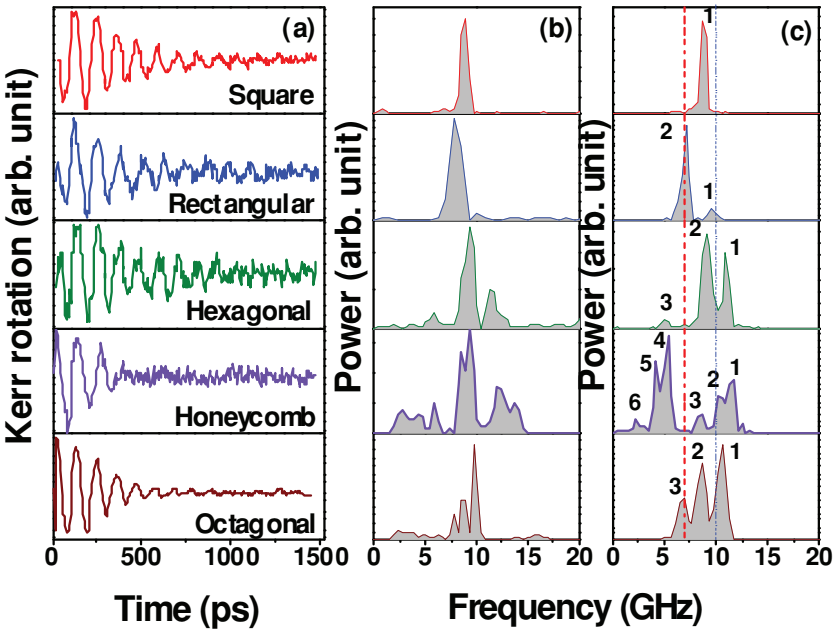

Figure 3. a) Experimental time-resolved Kerr rotation data and b) the corresponding FFT spectra are shown for Py dot lattices with five different lattice symmetry at H = 1.3 kOe at φ = 0°. c) FFT spectra of the simulated time-domain magnetization for five different lattice symmetry. The mode numbers are shown in the simulated FFT spectra, while the dashed vertical lines show the positions of the centre and edge modes of the simulated single dot with width = 100 nm and thickness = 20 nm.

lattices for different lattice symmetries can affect the modes. Simulations on square, hexagonal and honeycomb lattices with different shapes (flat and rough) of the boundaries do not affect the mode frequencies, although they do affect the relative intensities of the modes in the FFT spectra for the honeycomb lattice. The details of the simulation procedure are described in details elsewhere.[22,28] The samples were discretized into 2 nm × 2 nm × 20 nm cells and material parameters for Py were used as gyromagnetic ratio $\gamma = 18.5$ MHz/Oe, anisotropy field $H_k = 0$, saturation magnetization $M_s = 860$ emu/cc, and exchange stiffness constant $A = 1.3 \times 10^{-6}$ erg/cm. The material parameters were extracted by experimentally measuring the precession frequency (f) as a function of bias magnetic field (H) of a Py thin film of 20-nm thickness and by fitting the data with Kittel's formula for the uniform precession mode.

$$f = \frac{\gamma}{2\pi}\sqrt{(H + H_K)(H + H_K + 4\pi M_S)} \quad (1)$$

The lateral cell size is well below the exchange length of Py (5.3 nm). In general the widths and inter-element separations as observed in the SEM images are included in the simulation. The dynamic simulations were obtained for 1.5 ns at the time steps of 5 ps. Figure 3c shows the FFT spectra of the simulated time-domain magnetization, which qualitatively reproduce the experimental results. The relative intensities and the precise positions of the peaks in the frequency domains are not always quantitatively reproduced due to the limitations in the simulation. The average disagreements between the experimental and simulated mode frequencies are about 1%, 5.9%, 6.6%, 9% and 7.3% for square, rectangular, hexagonal, honeycomb and octagonal lattices, respectively. In addition, the splitting of the central peak for the honeycomb lattice and the low intensity band for the octagonal lattice below 5 GHz are not reproduced in the simulation. Further simulations with single dots with variation of dot size by up to ±10% and in lattices with variation of interdot separation by up to ±15% neither show any significant variation in the mode frequencies nor caused any mode splitting. Hence, the observed deviation is primarily because of the lack of inclusion of the precise edge roughness and other defects in the simulated samples as observed experimentally and the smaller size of the simulated lattices as opposed to the experimental lattices. Normally edge roughness of the dots is likely to randomize the magnetistatic stray field and lead to weakening of the effective stray field due to the averaging effect. It may also modify the edge modes and introduce additional localized modes within the dots by introducing additional pinning regions of magnetization. However, it is almost impossible to quantify the edge roughness and correlate it with the disagreement between the experimental and simulation results for large lattices. In addition, the optical excitation used experimentally is replaced by an estimated pulsed magnetic field in the simulation. Nevertheless, the important features of the experimental spectra are reproduced by the simulation.

2.2. Micromagnetic Analysis of the Collective Modes in the Lattices

We have further simulated the power and phase maps of various collective modes as observed both experimentally and in the simulation by using a home built code.[33] However, before that we have calculated the dynamics of a single Py nanodot of 100-nm diameter and 20 nm thickness. Two distinct peaks are observed, out of which the higher frequency peak is identified as the centre mode and the lower frequency peak as the edge mode of the dot[34,35] as shown in **Figure 4**. The centre and edge mode frequencies of the single 100-nm Py dots are shown as vertical dashed lines in Figure 3c. Clearly, the collective modes of various lattices are shifted in frequency with respect to the modes of a single dot and new modes appear in the hexagonal, honeycomb and octagonal lattices. In the square lattice one mode is suppressed, while the modes in the rectangular lattice are closest to those of a single dot. We have further simulated the power and phase maps for all resonant modes in different lattices as shown in **Figure 5** and **Figure 6**. The profile of the single mode in the square lattice is found to be the edge mode of the individual nanodots precessing coherently over the central part of the lattice, while the amplitude of precession dies out substantially near the vertical edges of the lattice. Due to the strong magnetostatic interaction the modes in the two central columns become completely uniform over the entire volumes of the nanodots. This is the dominant collective mode of the strongly coupled lattice as opposed to the weakly coupled arrays, where the centre and edge modes of the individual elements are generally observed.[34,35] It is evident from Figure 4 that the power of the edge mode is about five times higher than that of the centre mode of an individual 100-nm Py dot. In the square lattice due to very high magnetostatic interaction between the edge modes (they are much closer in distance to each other than the centre modes) they form a very strong collective mode, whose amplitude is sufficiently high to suppress the centre mode. For the rectangular lattice, mode 1 corresponds to the centre mode of the individual elements precessing coherently over the entire lattice except for the horizontal edges of the lattice. On the otherhand, mode 2 is the coherent precession of the edge modes of the individual nanodots over the lattice except for the vertical edges of the lattice. For the hexagonal lattice, mode

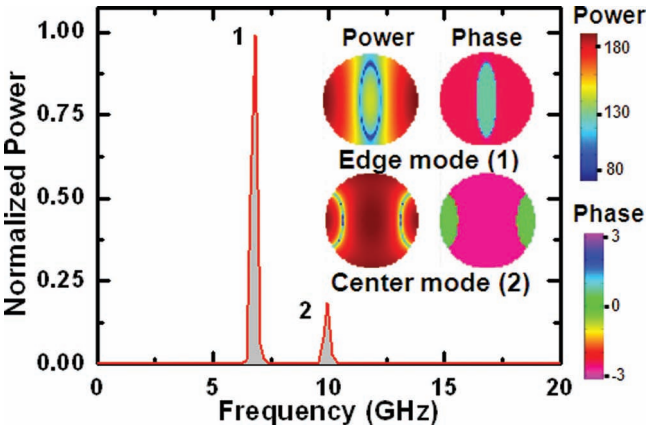

Figure 4. The power spectrum of the simulated magnetization dynamics of a single circular Py dot with 100-nm diameter and 20-nm thickness at $H = 1.3$ kOe. The power and phase maps of the two observed modes are shown in the inset. Mode 2 is identified as the centre mode while mode 1 as the edge mode of the Py dot.

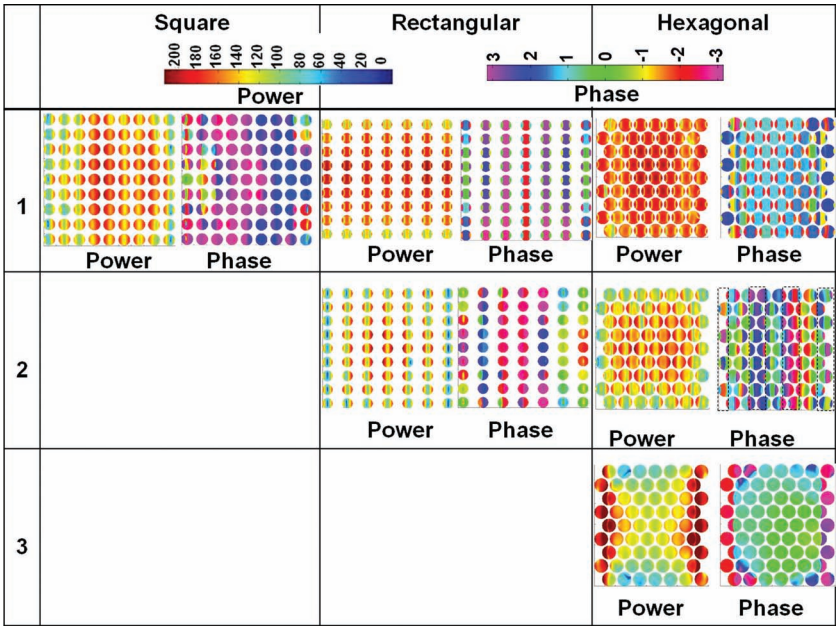

Figure 5. The power and phase maps for different precessional modes (as shown in Figure 3c) of Py dot lattices with square, rectangular and hexagonal symmetry. The colormaps for the power and phase distributions are shown at the top of the images.

1 corresponds to the coherent precession of the centre mode of the nanodots over the entire lattice with a slight dephasing near the vertical edges. Mode 2 corresponds to edge modes of the nanodots, which are precessing out of phase within consecutive stripe like regions marked by the vertical dotted lines. This mode is similar to the backward volume magnetostatic mode (BV) of the lattice. In mode 3, the dots are in phase, while the power on the dots reduces gradually from the vertical edges towards the centre of the lattice forming a bowtie like pattern. The honeycomb and octagonal lattices show very rich spectra and the corresponding mode profiles are shown in Figure 6. For the honeycomb lattice, mode 1 corresponds to the magnetostatic surface wave (SW) mode of the lattice, where consecutive rows are out of phase and alternative rows are in phase. Mode 2 is a mixed mode. Mode 3 corresponds to vertical stripe-like regions, where the half circles (full circle) are alternatively precessing in-phase and out-of-phase with each other. Mode 4 is localized within the centre of the lattice, which shows the BV mode of the individual dots. Mode 5 has its power reduced from the vertical edges towards the centre of the lattice and is out of phase with mode 4. Mode 6 is edge mode of the individual nanodots, which are primarily distributed in the even rows of the simulated lattice. This is because the edge to edge separations between the neighboring dots in the even rows are much larger than those in the odd rows. The strong magnetostatic interactions between the dots in the odd rows result in the disappearance of the edge modes in those rows. Mode 1 of the octagonal lattice is the centre mode of the nanodots, where they are collectively precessing in phase within the regions shown by the dotted boxes. Mode 2 is the BV mode of the nanodots localized within the same regions as for mode 1. Mode 3 is the edge mode of the individual nanodots uniformly distributed over the entire lattice.

To understand the origin of the differences in the spin wave spectra in different lattices, we have calculated the magnetostatic field distributions for lattices with different lattice symmetry as shown in **Figure 7**. Linescans of the simulated magnetostatic fields from various positions of the lattices as indicated by horizontal dashed lines in Figure 7 are shown in **Figure 8** alongwith the linescan of simulated magnetostatic field from a single 100-nm Py dot as a way of comparison. It is clear that both the internal fields on different dots as well as the stray fields are influenced by the lattice symmetry as well as the arrangement of the dots on a given lattice such as honeycomb and octagonal lattices. The overall internal fields inside the dots are increased significantly as compared to the single dot for all dots in the square and hexagonal lattices, while they increase only marginally in the rectangular lattice. For the honeycomb and octagonal lattices the internal fields inside the dots increase significantly as compared to the single dot for dots lying on the denser rows and do not increase significantly for the dots lying on the sparser rows. The above variation of the internal fields of the dots in various lattices alongwith the

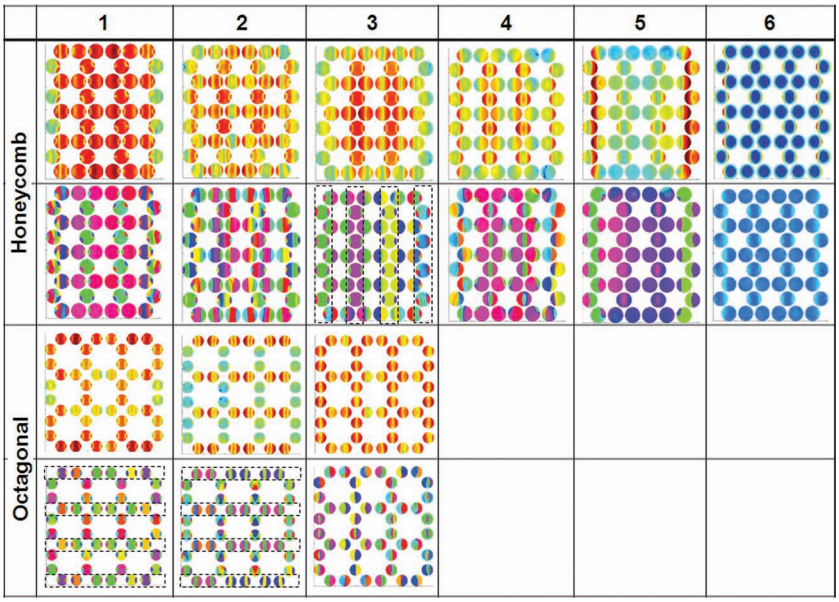

Figure 6. The power and phase maps for different precessional modes (as shown in Figure 3c) of Py dot lattices with honeycomb and octagonal symmetry. The colormaps for power (first and third rows) and phase (second and fourth rows) distributions are as shown in Figure 5.

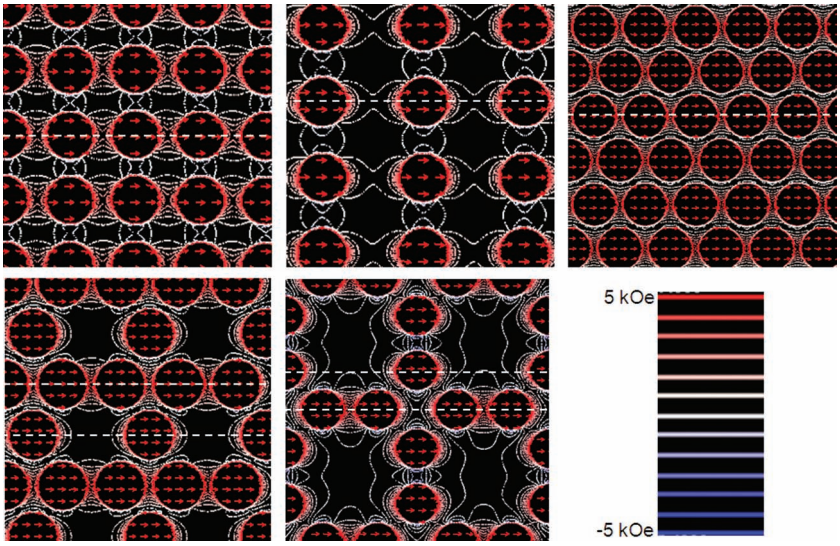

Figure 7. Contour maps of simulated magnetostatic field distributions (x-component) are shown for Py dots lattices with variable lattice symmetry at $H = 1.3$ kOe at $\varphi = 0°$. The arrows inside the dots represent the magnetization states of the dots, while the strengths of the stray magnetic fields are represented by the color bar at the lower right corner of the figure. The horizontal dashed lines show the positions of the lattices, from which the linescans are presented in Figure 8.

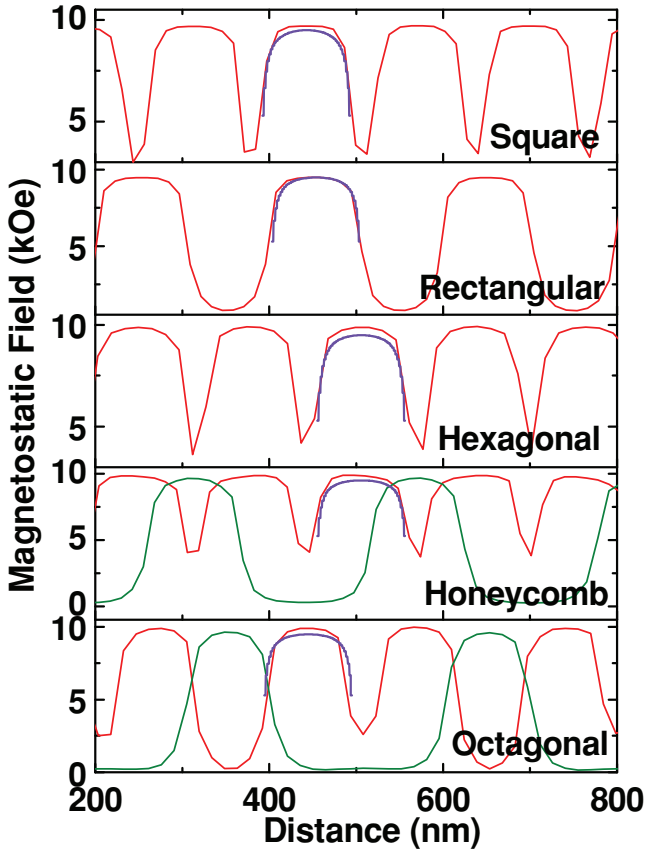

Figure 8. Linescans of simulated magnetostatic fields from various lattices as obtained from the positions indicated by horizontal dashed lines in Figure 7. Linescans of simulated magnetostatic field from a single dot is superposed on each panel for comparison.

stray fields are responsible for the variation in the frequencies of the collective modes as compared to the centre and edge mode frequencies of the single dot as shown in Figure 3. The stray field varies significantly with lattice symmetry primarily due to the arrangement of neighbouring dots in the lattice, as the boundary for every dot is almost identical in the simulation and the dots themselves are symmetric. Experimentally, there is some effect from the edge roughness and small differences in sizes and shapes from one dot to another. However, these effects are either introduced in the simulation (differences in size) or affect the dynamics only quantitatively, while the qualitative features of the spectra stems primarily from the lattice symmetry. For Bravais lattices (square, rectangular and hexagonal) dipolar contribution to the stray field is dominant but there are distinct differences due to the reasons stated as below. If we consider the columns standing perpendicular to the bias field, we see that for the square lattice the stray field is equally distributed on both sides of the columns as well as all elements on the columns are experiencing equivalent fields except for the edge elements. For the rectangular lattice the columns are separated by twice the distance of that of the square lattice causing a reduction of the stray fields between the columns but have similar amount of stray fields as the square lattice between the row elements. This caused two collective modes in the rectangular lattice. The hexagonal lattice is most closely packed and has the largest stray field and consequently shows a highly collective mode (mode 1). However, if we consider any column perpendicular to the bias field, it has alternative regions of interdot stray field or a full dot, which causes mode 2 in this lattice. However, for the honeycomb and octagonal lattices the stray field is even more complicated primarily because in the honeycomb lattice the unit cell has two nanodots, while there is a broken translational symmetry in the octagonal lattice. This causes unequal distributions of stray fields within the lattices and the occurrence of higher order multipolar contributions to the stray fields. Consequently, a larger number of modes with complicated profiles are observed in the honeycomb lattice. In the octagonal lattice also a band of modes are observed below 5 GHz experimentally but are not reproduced in the simulation possibly because the simulations are done on a much smaller lattice.

2.3. Anisotropy in Precessional Modes in the Hexagonal Lattice

Since the stray field and the resulting spin wave spectra can be controlled by varying the lattice symmetry for a fixed bias field, we further investigate the effect of varying the azimuthal angle φ of the bias magnetic field for a fixed strength of the magnetic field $H = 1.3$ kOe. This was done in the experiment by rotating the sample by a high precision rotary stage while keeping the microscope objective and the magnetic field constant. After

setting every value of φ, care was taken to ensure that the pump and the probe beams access the same region of the lattice. Here, we present the results from the hexagonal lattice as a case study as it belongs to the Bravais lattice and has the highest packing density. The time-resolved dynamics and the corresponding power spectra show significant variation with φ. The highest intensity peak (mode 2) in the power spectra shows a clear six-fold variation with the variation in φ, while the other modes for this lattice do not show any clear anisotropy with the variation in φ. **Figure 9**a shows the bias field dependences of mode 1 and mode 2 extracted from the experimental and simulated results alongwith the fits to the Kittel's formula. The extracted magnetic parameters from the fits are identical to those found earlier for the patterned thin film except that the saturation magnetization for mode 2 is significantly reduced (≈560 emu/cc) from that for mode 1 (860 emu/cc). This is because mode 2 corresponds to the collective dynamics of the edge modes of the individual nanodots, which is localized in strongly demagnetized regions near the edges of the dots. Figure 9b,c shows the variation of mode 2 with φ (symbols) extracted from the experimental and simulated results. The solid curves correspond to the fit to a harmonic field with six-fold anisotropy. The fit is reasonable for both cases, except that the peak to peak height is slightly lower in the experimental sample indicating lower value of the six-fold anisotropy. This is possibly due to the edge roughness and irregularities in the experimental samples, which averaged out the anisotropy arising due to the symmetry of the stray magnetic field in this lattice. We have further investigated the angular variation of the mode profile (power map) for mode 2, as shown in **Figure 10**, to understand the observed behavior. As discussed before for $\varphi = 0°$, mode 2 is the edge mode of the individual dots, which forms a BV like mode of the whole lattice. Consequently, the stray field is more effective on this mode as opposed to mode 1, where the individual dots show centre mode. In Figure 10, the overall power of the mode on the lattice represents the dynamic component of magnetization and the frequency of the mode directly depends on the net magnetization of the system. As the angle deviates from $\varphi = 0°$ the overall power of mode 2 decreases and attains a minimum at $\varphi = 30°$. For further increase in φ the power increase again and attains a maximum at $\varphi = 60°$. This phenomena is repeated and we observe maxima at $\varphi = 0°$, 60°, 120°, and 180° and minima at $\varphi = 30°$, 90°, and 150°. This periodic variation of power of mode 2 with φ is a manifestation of the variation of the magnetostatic field in the lattice (not shown), and it gets reflected in the six-fold variation in the frequency of mode 2.

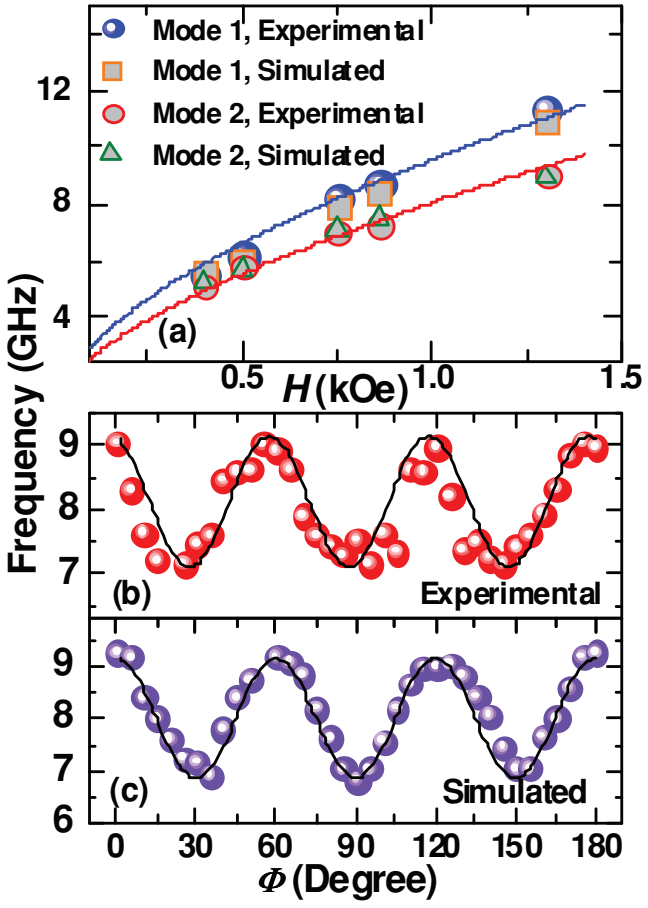

Figure 9. a) The variation of precession frequencies (mode 1 and mode 2) for a hexagonal lattice with the strength of the bias magnetic field at $\varphi = 0°$. Experimental and simulated results are shown by symbols, while the fits with the Kittel's equation are shown by the solid curves. The variation of mode 2 of the hexagonal lattice: b) experimental and c) simulation, as a function of the azimuthal angle φ of the in-plane bias magnetic field at $H = 1.3$ kOe. The symbols show the experimental and simulated results, while the solid curves show the fits with a harmonic function with six-fold symmetry.

3. Conclusions

We have fabricated closely packed Py nanodot lattices with 100-nm dot diameter and edge to edge inter-dot spacing of about 30 nm having variable lattice symmetry. We have chosen three two-dimensional Bravais lattices, namely the square, rectangular and hexagonal lattices and two non-Bravais lattices namely the honeycomb and octagonal lattices for this study. We have investigated the influence of lattice symmetry on the ultrafast magnetization dynamics of these lattices. The precessional dynamics have been induced and probed in an all-optical manner following an ultrafast demagnetization and a fast remagnetization. The dynamics has also been simulated by a time-dependent micromagnetic simulation method and the time-domain magnetization, power spectra, and the power and phase profiles of the resonant modes have been numerically calculated to get an extensive picture of the dynamics. The precessional modes of magnetization show significant variation with the variation of lattice symmetry. The square lattice shows a single uniform precessional mode, which is the coherent precession of the edge mode of all the dots in the lattice. The rectangular lattice shows two modes, which are coherent precession of the edge and centre modes of the dots over the entire lattice. The hexagonal lattice shows three clear modes, which correspond to the uniform collective mode, a BV like mode and a bowtie like mode of the whole lattice. The honeycomb lattice shows broad and rich spin wave spectrum, which includes various localized and extended modes including the SW mode of the lattice. For octagonal lattice three modes are observed, which are uniform,

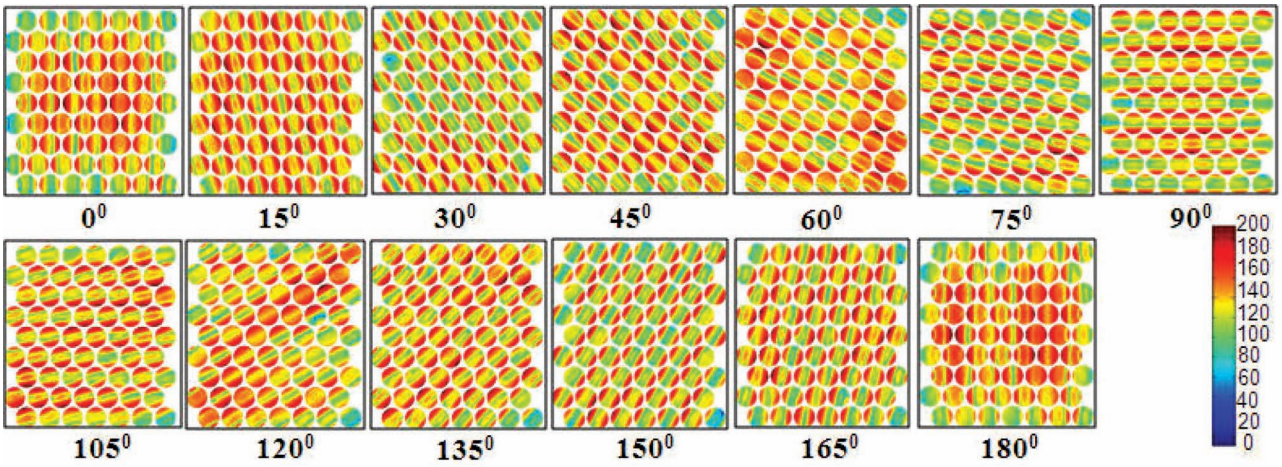

Figure 10. The power maps of mode 2 for the hexagonal lattice as a function of the azimuthal angle φ of the in-plane bias magnetic field at $H = 1.3$ kOe. The variation of the overall power on the entire lattice structure with φ indicates the variation of dynamic magnetization for this mode, which in turn gives the six-fold variation in the mode frequency.

SW like, and localized modes of the lattice. The magnetostatic fields within the lattices have been calculated, which helps in the interpretation of different observed modes of the lattices. The anisotropy of the collective modes in the hexagonal lattice has been investigated and mode 2, which is the edge mode of the dots forming a BV like collective mode of the lattice, shows a clear six-fold anisotropy, while other modes do not show any clear anisotropy with the variation of the azimuthal angle of the bias magnetic field. Analysis of the power profile of the anisotropic mode clearly shows the six-fold variation of the net dynamic component of magnetization with the azimuthal angle as a result of a similar variation of the magnetostatic field. The observed tunability in the magnonic spectra with varying lattice symmetry and the anisotropy of the magnonic modes with the variation of the orientation of the bias magnetic field may lead towards applications of the artificial nanomagnetic lattices as microwave filters, splitters and waveguide structures. Formation of composite artificial lattice structures with different lattice symmetries may lead to further tailoring of magnonic band structures for the above applications.

4. Experimental Section

Fabrication: Py dot lattices with varying lattice symmetry were prepared by a combination of electron-beam evaporation and electron-beam lithography. The beam current used during electron-beam lithography is 100 pA for a dose time of 1.0 µs. A bilayer MMA/PMMA (methyl methacrylate/poly methyl methacrylate) resist pattern was first prepared on self oxidized Si(100) substrate by using electron-beam lithography and Py was deposited on the resist pattern by electron-beam evaporation at a base pressure of about 1.3×10^{-7} Torr. A 5-nm-thick Al_2O_3 capping layer was deposited on top of the Py layer to protect the dots from general degradation with time as well as when exposed to the optical pump-probe experiments in air. This was followed by the lifting off of the sacrificial material and oxygen plasma cleaning of the residual resists that remained even after the lift-off process.

Measurement: The ultrafast magnetization dynamics was measured by a two-color optical pump-probe setup with simultaneous spatial and temporal resolutions of sub-µm and 100 fs, respectively. The second harmonic ($\lambda = 400$ nm, 10 mW, pulsewidth ≈ 100 fs) of a mode locked Ti-sapphire pulsed laser (Tsunami, Spectra physics, pulsewidth ≈ 70 fs) is used to excite the sample. The fundamental laser beam ($\lambda = 800$ nm, 2 mW) is used to probe the dynamics after passing through a variable time delay by measuring the polar Kerr rotation using a balanced photodiode detector, which completely isolates the Kerr rotation and reflectivity signals. The pump and probe beams are made collinear and are focused on each lattice through the same microscope objective with N.A. = 0.65. At the focal plane of the probe (diameter ≈ 800 nm), i.e., on the sample surface, the pump beam is slightly defocused, and has a larger diameter (≈1 µm) than the probe beam, which makes it easier to overlap the pump and probe beams on the sample surface. The probe beam is centred on the pump beam so that slight misalignment during the course of the experiment does not affect the pump-probe signals. The pump and probe beams were placed at the centre of each lattices and about 65 elements were measured for the square and hexagonal lattices while about 50 elements were measured for the rectangular and honeycomb lattices. Less than 50 elements were measured in the octagonal lattice, which is the sparsest lattice of all. A large enough magnetic field is first applied at a small angle (10–15°) to the planes of the lattices to saturate their magnetization. The magnetic field strength is then reduced to the bias field value (H = component of bias field in the sample plane), which ensures that the magnetization still remains saturated along the bias field direction. The pump beam was chopped at 2 kHz frequency and a phase sensitive detection of total reflectivity and Kerr rotations were made using lock-in amplifiers. The sample is scanned under the focused laser spots by using a piezoelectric scanning stage (x-y-z) with feedback loop for better stability. During the course of the experimental data accumulation the probe beam remained within the excitation area of the pump beam, while the sample drift is very small due to the feedback loop used in the scanning stage.

Supporting Information

Supporting Information is available from the Wiley Online Library or from the author.

Acknowledgements

The authors gratefully acknowledge the financial supports from the Department of Science and Technology, Government of India under

Grant Nos. SR/NM/NS-09/2007, INT/EC/CMS (24/233552), INT/JP/JST/P-23/09 and SR/WOS-A/PS-27/2010, Department of Information Technology, Government of India under grant no. 1(7)/2010/M&C, and Japan Science and Technology Agency Strategic International Cooperative Program under Grant No. 09158876. S.S. and B.R. would like to acknowledge the University Grants Commission, Government of India for financial support. D.K. would like to acknowledge the financial support from Council for Scientific and Industrial Research, Government of India for a Senior Research Fellowship (File ID: 09/575/(0090)/2011 EMR-I).

Received: September 5, 2012
Revised: October 26, 2012
Published online: December 17, 2012

[1] T. Thomson, G. Hu, B. D. Terris, *Phys. Rev. Lett.* **2006**, *96*, 257204.
[2] S. Tehrani, E. Chen, M. Durlam, M. DeHerrera, J. M. Slaughter, J. Shi, G. Kerszykowski, *J. Appl. Phys.* **1999**, *85*, 5822.
[3] D. A. Allwood, G. Xiong, C. C. Faulkner, D. Atkinson, D. Petit, R. P. Cowburn, *Science* **2005**, *309*, 1688.
[4] D. B. Carlton, N. C. Emley, E. Tuchfeld, J. Bokor, *Nano Lett.* **2008**, *8*, 4173.
[5] S. H. Chung, A. Hoffmann, S. D. Bader, C. Liu, B. Kay, L. Makowski, L. Chen, *Appl. Phys. Lett.* **2004**, *85*, 2971.
[6] B. Rana, S. Pal, S. Barman, Y. Fukuma, Y. Otani, A. Barman, *Appl. Phys. Express* **2011**, *4*, 113003.
[7] V. V. Kruglyak, P. S. Keatley, A. Neudert, R. J. Hicken, J. R. Childress, J. A. Katine, *Phys. Rev. Lett.* **2010**, *104*, 027201.
[8] G. N. Kakazei, Yu. G. Pogorelov, M. D. Costa, T. Mewes, P. E. Wigen, P. C. Hammel, V. O. Golub, T. Okuno, V. Novosad, *Phys. Rev. B* **2006**, *74*, 060406(R).
[9] R. Zivieri, F. Montoncello, L. Giovannini, F. Nizzoli, S. Tacchi, M. Madami, G. Gubbiotti, G. Carlotti, A. O. Adeyeye, *Phys. Rev. B* **2011**, *83*, 054431.
[10] G. Gubbiotti, M. Madami, S. Tacchi, G. Carlotti, T. Okuno, *J. Appl. Phys.* **2006**, *99*, 08C701.
[11] Z. K. Wang, H. S. Lim, V. L. Zhang, J. L. Goh, S. C. Ng, M. H. Kuok, H. L. Su, S. L. Tang, *Nano Lett.* **2006**, *6*, 1083.
[12] S. Tacchi, M. Madami, G. Gubbiotti, G. Carlotti, H. Tanigawa, T. Ono, M. P. Kostylev, *Phys. Rev. B* **2010**, *82*, 024401.
[13] S. Neusser, D. Grundler, *Adv. Mater.* **2009**, *21*, 2927.
[14] A. V. Chumak, V. S. Tiberkevich, A. D. Karenowska, A. A. Serga, J. F. Gregg, A. N. Slavin, B. Hillebrands, *Nat. Commun.* **2010**, *1*, 141.
[15] B. Lenk, H. Ulrichs, F. Garbs, M. Münzenberg, *Phys. Rep.* **2011**, *507*, 107.
[16] Y. Au, M. Dvornik, O. Dmytriiev, V. V. Kruglyak, *Appl. Phys. Lett.* **2012**, *100*, 172408.
[17] S. Kaka, M. R. Pufall, W. H. Rippard, T. J. Silva, S. E. Russek, J. A. Katine, *Nature* **2005**, *437*, 389.
[18] Z. Zeng, P. K. Amiri, I. N. Krivorotov, H. Zhao, G. Finocchio, J. P. Wang, J. A. Katine, Y. Huai, J. Langer, K. Galatsis, K. L. Wang, H. W. Jiang, *ACS Nano* **2012**, *6*, 6115.
[19] G. M. Müller, G. Eilers, Z. Wang, M. Scherff, R. Ji, K. Nielsch, C. A. Ross, M. Münzenberg, *New J. Phys.* **2008**, *10*, 123004.
[20] L. Giovannini, F. Montoncello, F. Nizzoli, *Phys. Rev. B* **2007**, *75*, 024416.
[21] R. Zivieri, R. L. Stamps, *Phys. Rev. B* **2006**, *73*, 144422.
[22] A. Barman, S. Barman, *Phys. Rev. B* **2009**, *79*, 144415.
[23] S. M. Weekes, F. Y. Ogrin, P. S. Keatley, *J. Appl. Phys.* **2006**, *99*, 08B102.
[24] L. Thevenard, H. T. Zeng, D. Petit, R. P. Cowburn, *J. Appl. Phys.* **2009**, *106*, 063902.
[25] C. C. Wang, A. O. Adeyeye, N. Singh, *Nanotechnology* **2006**, *17*, 1629.
[26] S. Tacchi, M. Madami, G. Gubbiotti, G. Carlotti, A. O. Adeyeye, S. Neusser, B. Botters, D. Grundler, *IEEE Trans. Magn.* **2010**, *46*, 1440.
[27] R. P. Cowburn, A. O. Adeyeye, M. E. Welland, *Phys. Rev. Lett.* **1998**, *81*, 5414.
[28] B. Rana, D. Kumar, S. Barman, S. Pal, Y. Fukuma, Y. Otani, A. Barman, *ACS Nano* **2011**, *5*, 9559.
[29] M. van Kampen, C. Jozsa, J. T. Kohlhepp, P. LeClair, L. Lagae, W. J. M. de Jonge, B. Koopmans, *Phys. Rev. Lett.* **2002**, *88*, 227201.
[30] A. Barman, S. Wang, J. D. Maas, A. R. Hawkins, S. Kwon, A. Liddle, J. Bokor, H. Schmidt, *Nano. Lett.* **2006**, *6*, 2939.
[31] E. Beaurepaire, J.-C. Merle, A. Daunois, J.-Y. Bigot, *Phys. Rev. Lett.* **1996**, *76*, 4250.
[32] M. Donahue, D. G. Porter, *OOMMF User's guide, version1.0, Interagency Report NISTIR 6376*, National Institute of Standard and Technology, Gaithersburg, MD, **1999**, http://math.nist.gov/oommf (accessed December 2012).
[33] D. Kumar, O. Dmytriiev, S. Ponraj, A. Barman, *J. Phys. D: Appl. Phys.* **2012**, *45*, 015001.
[34] J. Jorzick, S. O. Demokritov, B. Hillebrands, M. Bailleul, C. Fermon, K. Y. Guslienko, A. N. Slavin, D. V. Berkov, N. L. Gorn, *Phys. Rev. Lett.* **2002**, *88*, 047204.
[35] J. M. Shaw, T. J. Silva, M. L. Schneider, R. D. McMichael, *Phys. Rev. B* **2009**, *79*, 184404.